Directed Energy Transfer from Monolayer WS_2 to near Infrared Emitting PbS-CdS Quantum Dots

Arelo O.A Tanoh[1,2], Nicolas Gauriot[1], Géraud Delport[1], James Xiao[1], Raj Pandya[1], Jooyoung Sung[1], Jesse Allardice[1], Zhaojun Li[1], Cyan A. Williams [2,3], Alan Baldwin[1], Samuel D. Stranks[1,4], Akshay Rao[1*]

[1]Cavendish Laboratory, Cambridge, JJ Thomson Avenue, CB3 0HE, Cambridge, United Kingdom

[2]Cambridge Graphene Centre, University of Cambridge, 9 JJ Thomson Avenue, Cambridge, CB3 0FA, Cambridge, United Kingdom

[3]Department of Chemistry, University of Cambridge, Lensfield Rd, CB2 1EW, Cambridge, United Kingdom

[4]Department of Chemical Engineering & Biotechnology Department of Chemical Engineering & Biotechnology, University of Cambridge, Philippa Fawcett Drive, Cambridge CB3 0AS, UK.

*E-mail: ar525@cam.ac.uk

Abstract

Heterostructures of two-dimensional (2D) transition metal dichalcogenides (TMDs) and inorganic semiconducting zero-dimensional (0D) quantum dots (QDs) offer useful charge and energy transfer pathways which could form the basis of future optoelectronic devices. To date, most has focused on charge transfer and energy transfer from QDs to TMDs, *i.e.* from 0D to 2D. Here, we present a study of the energy transfer process from a 2D to 0D material, specifically exploring energy transfer from monolayer tungsten disulphide (WS_2) to near infrared (NIR) emitting lead sulphide-cadmium sulphide (PbS-CdS) QDs. The high absorption cross section of WS_2 in the visible region combined with the potentially high photoluminescence (PL) efficiency of PbS QD systems, make this an interesting donor-acceptor system that can effectively use the WS_2 as an antenna and the QD as a tuneable emitter, in this case downshifting the emission energy over hundreds of milli electron volts (meV). We study the energy transfer process using photoluminescence excitation (PLE) and PL microscopy, and show that 58% of the QD PL arises due to energy transfer from the WS_2. Time resolved photoluminescence (TRPL) microscopy studies show that the energy transfer process is faster than the intrinsic PL quenching by trap states in the WS_2, thus allowing for efficient energy transfer. Our results establish that QDs could be used as tuneable and high PL efficiency emitters to modify the emission properties of TMDs. Such TMD/QD heterostructures could have applications in light emitting technologies, artificial light harvesting systems or be used to read out the state of TMD devices optically in various logic and computing applications.

keywords: *two-dimensional, transition metal dichalcogenide, zero-dimensional, quantum dot, tungsten disulphide, lead sulphide-cadmium sulphide, energy transfer*

Monolayer transition metal dichalcogenides (TMDs), which are derived from their layered bulk crystals *via* dry mechanical cleavage[1] or liquid phase exfoliation[2,3] have attracted a great deal of research interest due to their distinctive optical, electronic and catalytic properties.[4–6] Monolayer TMDs can also be obtained *via* epitaxial growth methods, in particular chemical vapour deposition (CVD),[7,8] which is an area of ongoing research. A number of monolayer TMDs such as tungsten disulphide (WS_2) have a direct optical gap.[5] This property compounded with high absorption coefficients, high carrier mobilities[5] and potentially high photoluminescence quantum efficiency[9-11] (PLQE) promise great potential for their application in optoelectronic devices namely photodetectors, light emitting diodes (LEDs) and photovoltaics (PV).[12] The reduced dielectric screening in the monolayer limit compared to their bulk counterparts gives rise to tightly bound electron-hole pairs (*i.e.* excitons) with binding energies of the order of hundreds of meV at room temperature.[13,14] As a consequence, monolayer TMDs provide a convenient medium to study diverse excitonic species that arise *via* exciton-exciton or exciton-charge interaction.[13,15–17] Alternatively, these tightly bound excitons can be funnelled to other fluorescent media where they recombine radiatively at lower energy, thus tuning the emission properties of TMD excitons. Nanocrystal quantum dots (QDs), for example, provide a convenient, colour tuneable high PLQE emission medium[18,19] to which transferred 2D TMD excitons might be funnelled.

The exciton funnelling *i.e.* nonradiative energy transfer (ET) process can occur *via* two main mechanisms, namely Förster resonance energy transfer[20] (FRET) and Dexter energy transfer (DET).[21] FRET is a long-range process (~1-11 nm)[20] that occurs *via* dipole-dipole coupling, where the electromagnetic near-field of an oscillating transition dipole in the donor induces a transition dipole in the acceptor. Consequently, FRET between donor and acceptor systems is dependent on their physical separation and to a large extent, the overlap of emission and absorption spectra.[20-22] On the other hand, DET involves direct simultaneous tunnelling of electron hole pairs from the donor to acceptor due to donor-acceptor charge orbital overlap. As such, DET is strongly distance dependent and requires extremely close proximity between donor and acceptor molecules (≤ 1nm).[21,23]

A considerable amount of research into 2D-QD heterostructures has focused on interfacial charge transfer (CT) between QDs and monolayer TMDs for applications in photodetectors[24–31] and phototransistors.[32,33] To date, studies on energy transfer in 2D-QD heterostructures for light harvesting and light sensing applications have mainly focused on 0D-2D exciton transfer where monolayer TMDs or graphene are used as efficient exciton sinks to which optically or electrically generated excitons from QD emitters are non-radiatively transferred.[22,30,34–39]

Here, we demonstrate efficient ET from 2D TMDs to 0D QDs. We present a down–shifting heterostructure system, where monolayer tungsten disulphide (WS_2) acts as an antenna from which optically generated excitons are funnelled to lower energy lead sulphide-cadmium sulphide (PbS-CdS) near infrared (NIR) QD emitters. Photoluminescence excitation (PLE) studies confirm 2D-0D ET. Probing the underlying photophysics *via* time resolved optical microscopy reveals a fast, non-radiative ET process that out-competes intrinsic exciton trapping in monolayer WS_2. These results establish ET from 2D TMDs to 0D QDs as an efficient means to control excitonic behaviour, allowing for tuning of emission energies and construction of artificial light-harvesting systems.

Results & Discussion

Figure 1.a (1-6) shows the sample fabrication process from the initial exfoliated monolayers to the heterostructure. Following monolayer WS_2 exfoliation, a single QD layer was deposited on the sample surface using a conventional layer-by-layer method:[40-41] A linker layer of 1,3 benzendithiol (BDT) was first deposited *via* spin-coating to ensure strong adhesion of QDs on the sample surface; A low concentration (0.5 mg ml^{-1}) of oleic acid (OA) capped PbS-CdS QDs was then spun onto the sample and; Excess nanocrystal and ligand material was rinsed off by spin-coating toluene, leaving a single layer of QD film. Sample preparation is detailed further in the *experimental methods* section. Figure 1.b. illustrates the process of exciting the 2D material with high energy visible photons forming excitons that funnel to the QDs where they recombine and emit lower energy NIR photons. Figure 1.c. shows the absorption and PL spectra of a WS_2 monolayer. The absorption spectrum of WS_2 monolayer (light blue circles) clearly reveals `A', `B' and `C' excitonic peaks positioned at 2.0 eV (617 nm), 2.4 eV (512 nm) and 2.88 eV (430 nm) respectively. The PL spectrum (dark blue dashed line) is well overlapped with the A exciton band. The absorption and PL spectra of the QDs in colloidal suspension are plotted in Figure 1.d. The colloidal PbS-CdS absorption spectrum (solid black line) reveals an absorption peak at 1.76 eV (704 nm) while the PL spectrum (black dotted line) exhibits the red-shifted peak position at 1.38 eV (900 nm). Interestingly and importantly, the WS_2 PL lies within PbS-CdS absorption spectrum, which is a key requirement for efficient FRET. Consequently, we chose PbS-CdS QDs and WS_2 monolayer as an efficient energy transfer pair.

An additional factor considered was the absorption cross sections of the constituent donor and acceptor materials. The TMD monolayer's role as an optical antenna and exciton generation medium requires that it has a higher absorption cross section compared with the nanocrystal emitter. While the absorption cross sections of monolayer tungsten disulphide (WS_2) and other TMDs in the visible region are not very well documented, the absorption coefficient σ_{gs} of few layer (1-3 monolayers) MoS_2 obtained from a study on non-linear optical performance of MoS_2 films by Zhang *et al*[2] gives a value of σ_{gs} = 4.7 x 10^{-15} cm^2 for 515 nm pulsed excitation. We estimate the absorption cross section for a MoS_2 monolayer simply by dividing σ_{gs} = 4.7 x 10^{-15} cm^2 by the maximum number of layers (*n = 3*) in the sample quoted to give $\boldsymbol{\sigma_{gs} \approx 1.6 \times 10^{-15}\ cm^2}$ at 515 nm. We note that the absorption of monolayer WS_2 is similar in magnitude to MoS_2 at 515 nm[42] and hence estimate that their absorption cross sections are comparable at 515 nm. Moreover, considering the transition from indirect to direct optical gap from few layer to monolayer TMD, the actual value of absorption cross section should exceed this estimation. Following Cademartiri *et al.*,[43] we compute the absorption cross section of a single QD *via* Equation *1* using the molar extinction coefficient, ε_A [M^{-1} cm^{-1}] estimated in supplementary information (SI) section 3.2. Units are provided in square brackets for clarity.

$$\sigma = \frac{2303\ [cm^3 L^{-1}]}{N_A\ [mol^{-1}]} \varepsilon_A(\lambda)\ [L\ mol^{-1} cm^{-1}] \quad (1)$$

Where N_A is the Avogadro number. This yields a value of $\boldsymbol{\sigma \approx 8.74 \times 10^{-17}\ cm^2}$ at 515 nm. Given the estimations made and the shape of the monolayer WS_2 absorption spectrum (Figure 1.c), we consider that the WS_2 absorption cross-section exceeds that of the QDs by a large factor in the ~ 400 nm – 650 nm range.

As shown in the Figure 1.b, steady state PL microscopy was performed with the sample placed upside down to directly excite the monolayer WS_2 first *via* the thin glass slide, avoiding shadowing by the QDs. Directly exciting the monolayer ensures efficient generation and funnelling of TMD excitons to the QDs as illustrated in Figure 1.b (inset). This results in considerable QD PL enhancement in the heterostructure as subsequently discussed in detail for Figure 1.e. Exciting the QDs directly would otherwise cause sub-optimal exciton generation and funnelling from the monolayer TMD due to absorption of a proportion of incoming photons by the shadowing QDs, amounting to less prominent QD PL enhancement. The steady state confocal PL spectra of QD film on the bare substrate (black) and the heterostructure (red) are plotted in Figure 1.e. While the QD film on the bare substrate shows a broad Gaussian PL peak in the NIR region centred at 1.38 eV (900 nm), the heterostructure exhibits two distinctive PL peaks *i.e.* the narrow WS_2 PL peak in the visible region centred at 2.0 eV (~619 nm) and a broad QD PL peak in the NIR region at 1.42 eV (870 nm). We note that the QD PL spectrum of the heterostructure is blue-shifted by 30 nm and enhanced by a factor of 2.6. The observed blue shift in the heterostructure's QD PL on the WS_2 monolayer compared to the bare substrate may be attributed to the following possibilities: i) a difference in dielectric environment between the surfaces; ii) a difference in QD aggregation concentration of the QD film between the surfaces or; iii) a combination of both factors. We also note that it is possible that the PL yield of the QDs on the WS_2 monolayer is higher than those on the bare substrate as a result of the aforementioned factors. While ascertaining the nature of the heterostructure's surface morphology and dielectric properties could offer additional explanation towards the observed changes in QD emission properties between the bare substrate and TMD monolayer surface, the scope of this work is confined to investigating the possibility of ET of WS_2 excitons to the QDs as evidenced by the QD PL enhancement on the monolayer surface. [21] Hence, we seek to verify the notion of 2D→ QD ET *via* further optical characterization studies.

Figure 2.a. shows the optical micrograph (left) of a WS_2 flake and confocal NIR (QD) PL map (right) from the same region obtained upon excitation at 514.5 nm. The colour bar represents the PL integral in the 780 - 960 nm spectral range. Enhanced NIR PL from QDs is obtained in the vicinity of the monolayer (dashed line) whereas QD PL in the bulk flakes (solid line) is quenched. The difference in NIR PL intensity between monolayer and bulk flakes suggests that the WS_2 monolayer serves as the ET donor, while the bulk quenches excitons. Figure 2.b. shows the QD PL spectra from the heterostructure (red) and bare substrate (black) extracted from points marked `*x*' on the QD PL map in Figure 2.a., RHS. Lime green dashed lines are single Gaussian peak fits. The QD PL spectrum of the heterostructure is blue-shifted by 47 nm compared with the QD on bare substrate. We also observe a QD PL enhancement of 5.2x, which we attribute to energy funnelling from the directly excited WS_2 monolayer. To delve into the possibility of ET from the WS_2 monolayer to PbS-CdS QDs we employ wide-field photoluminescence excitation (PLE) microscopy. We recorded the PL intensity integrated over the NIR region (800-1000 nm), exclusively corresponding to PL from the QDs, and scanning the excitation wavelength across 560 - 700 nm, mainly resonant to WS_2 at low fluence (c.a., ~0.006 $\mu J/cm^2$ at 620 nm). The PLE spectra shown in Figure 2.c were taken on the heterostructure (red) and in an area with QDs only (black) away from the heterostructure. We note that the PLE data is normalised with respect to the mean PLE values at wavelengths off-resonant to the WS_2 donor (670 -700 nm) to account for the increase in QD emission due to resonant 2D → QD ET only, discounting the effects of other previously discussed factors that may contribute to improved QD emission on the heterostructure. The unscaled PLE data for Figure 2.c. is included in the supporting information, SI

section 1. Unlike the PLE spectrum of QD only area (black), the PLE spectrum of the heterostructure (red) clearly reveals the signature `A' excitonic peak centred at 616 nm (~2.0 eV), indicative of a significant contribution from the WS_2. Furthermore, as shown in Figure 2.d., the resulting PLE spectrum (red line) obtained by subtracting the normalised QD PLE spectrum (Figure 2.c., black) from that of heterostructure (Figure 2.c., red) is almost perfectly overlapped with a typical WS_2 absorption spectrum (blue circles). This is strong evidence that energy transfers from WS_2 monolayer to the QDs. In order to accurately quantify ET from WS_2 monolayer to QD, we calculated the photoluminescence contribution, PL_{ctr} as a function of excitation wavelength using PLE data shown in Figure 2.c. The key assumption in the derivation of PL_{ctr} is informed by Vavilov's rule,[44] which states that PLQE is independent of excitation wavelength. QD PLQE is hence regarded as constant. This is considered as a reasonable assumption for the wavelength range presented in the PLE data (560 – 680 nm). Further details on the derivation of PL_{ctr} are given in SI section 2. As shown in Figure 2.e., PL_{ctr} is maximized at 616 nm with a value of 58% and reduces considerably thereafter at lower energy excitation energy. Additionally, we carried out PLE measurement on a series of heterostructures with various QD-2D surface attachment thiol ligands. As well as the heterostructure based on 1,3 benzenedithiol (BDT) reported in herein, 1,4 butanedithiol (BuDT) and 1,6 hexanedithiol (HDT) were also studied. SI section 3.1 provides a brief PLE study of the heterostructures based on the different ligands. From this we note here that all heterostructures measured show ET from 2D to QD.

All surface attachment ligands used are of lengths < 1 nm, and thus in principle lie within range for ET *via* tunnelling *i.e.* DET. Although orbital overlap between the monolayer TMD donor and QD acceptor is a possibility at such separation distances, their respective large oscillator strengths highly favours ET *via* FRET[21] over DET. In SI section 3.2, we estimated the theoretical Förster radius of $\boldsymbol{R_0 \approx 6.5\ nm}$, which exceeds the lengths of the ligands used. This result emphasizes the significance of the combined oscillator strengths of the constituent heterostructure materials (*i.e.* TMD donor and QD acceptor) over their physical separation, even at low proximity, which strongly suggests FRET as the dominant ET mechanism observed in the heterostructures measured. In addition, while short ligands such as BDT have previously been shown to improve CT between QDs,[45] the CdS shell encapsulating the PbS core has been shown to suppress CT.[46]

To gain further insight into the dynamics of the ET process observed from PLE we turn to time resolved PL (TRPL) microscopy, where we detected changes in emission decay from WS_2 using a 509 nm pulsed laser excitation. Excitation was filtered from the detection line with a 510 nm long pass filter, while QD emission was removed using a 700 nm short-pass filter, allowing for WS_2 monolayer PL detection only. To distinguish bare WS_2 from WS_2 in the heterostructure, we refer to the former as `pristine' WS_2.

Figure 3.a shows the normalised time resolved PL decay signals of the pristine monolayer and heterostructure under low fluence excitation (0.01 μJ cm^{-2}). The transient PL profile of pristine WS_2 shows a bi-exponential decay profile consisting of fast and slow components. On the other hand, we observe that the fast component of the heterostructure's PL profile is quenched below the detector's initial response function (IRF). The two PL decay components observed in the pristine monolayer can be attributed to direct band-edge to ground state excitons transitions and exciton trapping respectively.[11] In contrast, the much faster PL kinetics observed in the heterostructure suggests an additional efficient fast decaying process present in this system. In fact, this quenching observed in the heterostructure is in accordance with what is expected of the PL dynamics of the donor in a

nonradiative ET system. Figure 3.b. shows an excitation fluence series performed on both pristine and heterostructure samples. The pristine case shows a general increase in PL lifetime with fluence, which is indicative of `trap' or `defect' state filling. This trap limited behaviour has also been observed in WS_2 and MoS_2 monolayers treated with bis(trifluoromethane)sulfonimide (TFSI).[47,11] The apparent increase in the fast component of the PL lifetime with fluence is due to trapping and detrapping of excitons to the band edge prior to recombination to the ground state. The long-lived component is due to radiative transitions from the trap to ground state.[47] Increasing the excitation fluence would lead to saturation of trap states, forbidding further trapping and promoting dominant band-edge to ground state recombination. The fluence series presented in Figure 3.b however lies below trap-state saturation. This is given by the increasing fast PL component lifetimes as a function of fluence. Trap-state saturation would otherwise be characterized by a constant fast PL component with increasing excitation fluence. Further increases in fluence would lead to an eventual reduction fast PL component lifetime, signalling the onset of exciton-exciton annihilation. Interestingly, in the heterostructure case, the fast PL components are quenched below the IRF throughout the series. This outcome suggests that ET rate outcompetes the intrinsic exciton trapping rate in monolayer WS_2, which occurs on a time scale of few picoseconds.[48,47] We therefore predict that the 2D→QD ET rate occurs on a faster or similar time-scale.

The observation of a concomitant growth in QD PL lifetime with WS_2 PL quenching would provide further confirmation of ET. However, as recently discussed, it is likely that the ET process occurs on a timescale faster than intrinsic trapping in the monolayer TMD (*i.e.* few ps), too fast to be detected by time-correlated single photon counting (TCSPC) as employed in this study, and perhaps even too fast for Streak Camera measurements. As further confirmation of this hypothesis, Figure 4 shows the normalised time resolved PL (TRPL) decay signals for a heterostructure (red) prepared on spectrosil compared with the QDs on the bare substrate (black). Excitation was provided using the 509 nm pulsed laser at 0.5 MHz repetition rate and 200 ps resolution. The excitation signal was filtered out using a 510 nm long pass filter and QD emission was isolated with an 800 nm long pass filter, removing any signal from the underlying WS_2. The heterostructure decay clearly shows the IRF component convoluted with the long-lived QD PL decay at early time. This indicates the occurrence of a phenomenon much faster than the sensitivity of the setup. Therefore, the expected increase in QD life-time due to ET from the underlying WS_2 occurs at a much earlier time than what is detectable by the TRPL setup available to us.

Steady state PL measurements provide information on the spectral changes that occur in the WS_2 monolayer PL from pristine to heterostructure case. Also, comparing steady state PL with TRPL data at similar excitation intensity provides better understanding of exciton recombination pathways in the heterostructure. Figure 5.a shows scatter plots of monolayer WS_2 (visible) PL integrals and the corresponding PL peak wavelengths extracted from spatial PL maps of the sample in pristine (blue) and heterostructure (red) form. This data was collected from a 64 μm *x* 48 μm rectangular region within the monolayer shown in Figure 2.a LHS. As far as practicable, PL measurements were taken in the same region before and after QD deposition. For further clarity the WS_2 PL collection region is shown in SI section 4. Maps were measured with 514 nm continuous wave (CW) laser excitation at 80.2 W cm^{-2} intensity for good signal to noise ratio. It is known that different types of excitons exist in atomically thin nanomaterials, *i.e.*, WS_2 monolayer. Accordingly, it is of importance to understand how different types of excitons behave and contribute differently when ET occurs. We begin with analysing steady state PL spectra as it gives an indication of the types of excitons present. Figure 5.b. shows the

PL spectra of an exemplary point on the monolayer in pristine (blue) and heterostructure (red) form. The spectra were deconvoluted with Gaussian peaks which represent the neutral exciton (NE) and lower energy species (X_2) such as trions, which are characterized by broad low energy features in monolayer TMD spectra.[11] X_2 may also arise from eventual radiative recombination of neutral excitons trapped in sub-gap states. Upon recombination to the ground state, these excitons can bind with electrons to form trions, which is known to occur in *n*-type TMDs such as WS_2.[11,49] Figure 5.c shows the fitted time resolved PL of pristine (blue) and heterostructure (red) cases at high excitation intensity (3.2 μJ cm^{-2} → 63.4 W cm^{-2}). Figure 5.d. shows the proposed radiative exciton recombination pathways resulting from the high intensity PL/TRPL comparison. Table 1 shows the fitted PL lifetimes (τ) of pristine and heterostructure samples at low and high intensity excitation and ET efficiencies. ET efficiencies were computed *via equation 2*. SI section 5 provides the full derivation of *equation 2*. Heterostructure lifetimes are denoted by an apostrophe. Given that the fast component of the heterostructure's WS_2 PL lifetime (τ_1') is limited by the IRF, the fitted values presented in table 1 represent an upper bound.

$$\eta_{ET} = 1 - \frac{\tau_1'}{\tau_1} \qquad (2)$$

Table 1: Fitted PL lifetimes of pristine and heterostructure samples and resulting estimates for ET efficiencies. Fast components of WS_2 PL decay in heterostructure $\boldsymbol{\tau_1'}$ and transfer efficiencies $\boldsymbol{\eta_{ET}}$ represent upper and lower bound values respectively due to limitations in instrument sensitivity. High intensity excitation values used for comparison with steady stat PL are italicised.

Intensity	Pristine τ_1	Heterostructure τ_1'	Pristine τ_2	Heterostructure τ_2'	η_{ET}
0.21 W cm^{-2}	0.456 ns	0.26 ns	3.63 ns	3.64 ns	42%
63.4 W cm^{-2}	*0.62 ns*	*0.26 ns*	*2.95 ns*	*2.9 ns*	*58%*

Statistical analysis of the scatter data in Figure 5.a. reveals an average PL quenching ΔPL_{AVE} 50% and spectral blue shift $\Delta\lambda_{AVE}$ of 7 nm from the pristine to the heterostructure case. The spectra in Figure 5.b shows that the *NE* component quenches by 50%, while X_2 quenches by 76%. An overall quenching of 67% was computed from the raw spectra. The large X_2 quenching helps to explain the spectral narrowing in the red signal and the general blue shift in Figure 5.a. Interestingly, the difference in quenching between the *NE* and X_2 species leaves 26% of quenched excitons unaccounted for. This implies an additional exciton recombination pathway. As X_2 may arise from slow exciton recombination from trap states, the excess quenching of X_2 excitons could be explained as non-radiative trap-QD transfer. Table 1 however reveals that the slow decay component (τ_2) associated with trap-ground state transition remains practically unchanged between the pristine and heterostructure case for a given excitation intensity, *i.e.* $\tau_2 \sim \tau_2'$. WS_2 trap state to QD exciton transfer requires that $\tau_2' < \tau_2$ and therefore negates this possibility. This suggests that the excess quenched excitons may dissipate *via* some other non-radiative pathway.

On the other hand, table 1 shows that fast component of the bi-exponential decay associated with neutral exciton recombination[11] is quenched by 58% from τ_1~0.62 ns in the pristine monolayer to τ_1' ~0.26 ns in the heterostructure case. This lies in close agreement to the 50% *NE* quenching estimated in steady state PL. The strong fast PL decay lifetime quenching shows that ET occurs *via* neutral excitons transitioning from the WS_2 band edge to the QD acceptor, while intrinsic exciton trapping in the donor and non-radiative losses compete with this process. This justifies the use of fast decay components (τ_1, τ_1') to compute the lower bound ET efficiencies shown in table 1 *via equation 2*. As previously highlighted, exciton trapping and detrapping in the donor gives rise to increasing τ_1 as a function of fluence, which manifests as an apparent increase in η_{ET} as a function of fluence. While non-radiative pathways are yet to be uncovered, passivating trap states to improve donor PLQE should lead to more efficient ET from the WS_2 donor band edge to the QD acceptor.

Figure 5.d provides a clear illustration of radiative exciton pathways in pristine (LHS) and heterostructure (RHS) cases, which is derived from the PL/TRPL comparison in Figure 5.b-c and supported by the TRPL fluence series in Figure 3.b. In pristine WS_2, upon excitation from the ground state a proportion of excitons instantaneously transition from the band edge to trap states on the order of few picoseconds[47] at trapping rate k_{TR}, while others recombine radiatively from the band edge to ground state at the rate k_D. Those excitons that are trapped in sub-gap states radiatively recombine to the ground state over long periods of the order of ns[47] at rate k_2. In the heterostructure, excitons preferentially transfer from the WS_2 band edge to the QD at rate k_{ET}, such that $k_{ET} > k_{TR}$, thus quenching the fast component τ_1 lifetime below the IRF. This also explains the sizeable quenching of X_2 in the steady state PL spectra as there are fewer excitons being trapped in the presence of an acceptor QD. Band edge excitons that are not trapped, transferred or lost *via* some other non-radiative process, recombine radiatively to the ground state at k_D over 10s – 100s of picoseconds,[48] which is below the instrument response. The remaining emission from direct band edge recombination as shown in Figure 5.b, strongly suggests that the 2D-QD transfer pathway becomes saturated. As with trap states, the QD band edge can become saturated, forbidding further incoming excitons, which may return to the WS_2 band-edge and radiatively recombine or dissipate *via* a non-radiative process as suggested by the `lost' quenched excitons identified from Figure 5.b.

To summarise the results from optical measurements presented, PLE studies confirm ET from monolayer 2D WS_2 to 0D QDs. Further PLE on heterostructures with differing surface attachment thiol ligands show ET. While all ligands lengths used lie within tunnelling distances favourable for DET (< 1 nm), the large oscillator strengths of the 2D TMD donor and QD acceptor favour FRET as given by the large theoretical Förster radius computed. The CdS shell surrounding the PbS core in the QDs provides an additional tunnelling barrier, thus supporting FRET as the dominant ET process observed. Time resolved PL studies further confirm non-radiative ET by virtue of strong quenching of donor WS_2 PL in the presence of the acceptor QDs. TRPL studies also strongly indicate that this transfer process is faster than intrinsic early time trapping of excitons in the WS_2 monolayer, which would otherwise lead to radiative or non-radiative exciton recombination *via* trap states in the pristine monolayer. Comparing high excitation intensity PL and TRPL measurements provides a clearer understanding of radiative recombination pathways for excitons in the TMD-QD heterostructure. The comparison implies that intrinsic exciton trapping in the TMD monolayer and a non-radiative process compete with ET from 2D to QD. Further analysis also suggests that the exciton transfer channel can become saturated at high excitation intensities.

Conclusions

In conclusion, we have demonstrated the ability to transfer excitons from monolayer WS_2 to NIR PbS-CdS QD emitters. PLE studies provide confirmation of ET, with 58 % of QD PL donated by monolayer WS_2. The large oscillator strengths of the donor TMD and acceptor QD lead to a large Förster radius, suggesting FRET as the dominant ET mechanism. TRPL studies reveal that the ET process is faster than intrinsic exciton trapping in monolayer WS_2. A comparative study between high excitation steady state PL and TRPL confirms exciton transfer from the WS_2 band edge to the PbS-CdS band edge, while intrinsic exciton trapping in the donor and other non-radiative channels act as competing pathways. Residual emission from the donor in the heterostructure suggests that the ET pathway can be saturated at high excitation intensities. Future studies of such heterostructures could provide a clearer understanding of non-radiative loss mechanisms *via* more sensitive methods such as femtosecond transient absorption (TA) and high resolution TRPL. Trap state passivation *via* monolayer TMD surface treatments can be used to drastically reduce exciton trapping rates, not only enhancing ET, but isolating non-radiative loss pathways so that they can be better understood. The TMD/QD heterostructures demonstrated here combine the high absorption cross-section or electrical injection and transport properties of monolayer TMDs, with the high quality and highly tuneable optical properties of QDs. The ability to tune emission properties of monolayer TMDs using high PLQE QD emitters has potential device applications in areas such as in light emitting technologies namely displays, solid-state lighting and lasers, [19,22] as well as artificial light harvesting systems. Such structures could also be used to read out the state of TMD devices optically in various logic and computing applications.

Experimental Methods

Sample Preparation

Monolayer Preparation

Thin 22 mm x 22 mm glass cover slides of thickness 170 µm were solvent processed *via* sonication in acetone and isopropyl alcohol (IPA) for 15 mins, dried with a nitrogen (N_2) gun and treated in oxygen (O_2) plasma to remove adsorbants. Large area WS_2 monolayers were prepared *via* gold-mediated exfoliation.[50] The bulk crystal was purchased from 2D Semiconductors and exfoliated manually onto low adhesion clean-room tape prior to depositing a thin gold layer (~100-150 nm) *via* thermal evaporation under vacuum conditions. Once gold was evaporated, thermal release tape was adhered atop the gold coated WS_2 and pealed, leaving exfoliated WS_2 on top of a layer of gold attached to the thermal release tape. With the WS_2 exfoliate facing downwards, the thermal tape was affixed to the target substrate and heated on a hot plate up to 125 °C. Once the thermal tape pealed leaving the WS_2 exfoliate sandwiched between the substrate and gold, the excess gold was removed by gently swirling the sample immersed in potassium iodide (KI_2) and iodine (I_2) standard gold for 6 minutes. Finally, the sample was rinsed in deionised water, then sonicated in acetone for 10 mins and rinsed in IPA for 5 mins. Samples were dried with a nitrogen (N_2) gun. Monolayers were identified using optical contrast method. [51]

PbS-CdS QD preparation

All chemicals were purchased from Sigma Aldrich or Romil and were used as received. The synthesis of PbS QDs was carried out following modified versions of the method of Hines & Scholes.[52]

Lead oxide (0.625 g, 99.999%), oleic acid (OA, 2 mL, 90%) and 1-octadecene (ODE, 25 mL, 90%) were placed in a three-necked round bottomed flask and degassed under vacuum at 110 °C for 2 hours with stirring, forming a colourless solution. Subsequently, the flask was put under nitrogen flow and heated to 80 °C. In a nitrogen glovebox, a syringe was prepared containing ODE (13.9 mL) and bis(trimethylsilyl)sulfide (TMS_2S, 296 µL, 95%). The syringe containing the sulfur precursor was rapidly injected into the reaction flask, which was allowed to cool. Upon cooling to 60 °C, the reaction mixture was transferred to an argon glovebox. The synthesised nanocrystals purified four times by precipitation with ethanol/1-butanol and acetone, centrifugation (10000 *g*) and resuspension in hexane/toluene. The purified QDs were redispersed in toluene for storage in an argon glovebox.

Cation exchange of PbS QDs was performed following a modified method of Neo *et al.*[53] A typical procedure was as follows:

Cadmium oxide (1.03 g, 99.999%), OA (6.35 mL) and ODE (25 mL) was placed in a three-necked round bottomed flask and degassed under vacuum for 110 °C. The vessel was switched to nitrogen and heated to 230 °C for 2 hours, resulting in the formation of a colourless solution of cadmium oleate. The solution was cooled and degassed under vacuum for 15 minutes. The flask was switched to nitrogen and the solution was transferred to a nitrogen glovebox for storage. The cadmium oleate precipitated at room temperature and was heated to 100 °C before use.

Cation exchange was performed with the addition of Cd-oleate solution to PbS nanocrystals. A typical reaction is as follows. In a nitrogen glovebox, a suspension of PbS nanocrystals in toluene (50 mg, 50 mg mL^{-1}) was heated to 100 °C. Cadmium oleate in ODE (0.35 mL, 0.26 M) was added to the nanocrystal suspension and maintained at 100 °C. The reaction was quenched after 1 minute with the

addition of anhydrous acetone. The cation-exchanged nanocrystals were twice precipitated, centrifuged and re-suspended with acetone and toluene.

Heterostructure Preparation

Heterostructures were prepared using the following steps: In a nitrogen (N_2) glovebox, the monolayers on substrate were spin coated at 1000 rpm for 50 seconds with 200 µL of 20 mM 1,3 benzene dithiol dissolved in acetonitrile forming a linker layer; 200 µL of 0.5 mg/ml PbS-CdS QDs ,with Oleic Acid surface attachment ligands suspended in toluene were deposited *via* spin coating at 500 rpm for 60 s; excess material was rinsed off by spin coating toluene on the sample at 500 rpm for 60 s. A waiting time of 5 minutes was observed between steps. Finally, the sample was encapsulated using a top 18 mm x 18 mm thin glass slide with double sided tape at the edges to hold the top slide in place. Gaps between the bottom and top glass slides were sealed with epoxy and left to dry over 24 hours in the N_2 environment.

It must be noted that the optical characterization (PL, PLE and TRPL) results presented in Figures 1-3 and 5 are based on the same monolayer in pristine and heterostructure form *i.e.* each measurement was performed before and after QD deposition.

Optical Characterization

Steady State Absorption and PL Spectroscopy

The absorption spectrum of the QDs was measured using a Shimadzu UV-VIS spectrometer. 0.1 mg/ml solution of colloidal QDs in toluene in a 1 cm cuvette was placed in an integrating sphere. A 1 cm cuvette filled with toluene was used as a reference. Steady state QD PL in Figure 1.c was obtained using a fluororemter (Edinburgh Instruments), with 0.1 mg ml^{-1} solution deposited in a 1 mm cuvette. Excitation wavelength was set to 500 nm and PL was detected with an indium gallium arsenide (InGaAS) array.

Steady state Absorption Microscopy

The absorption spectrum of monolayer WS_2 on quartz substrate was measured with a Zeiss axiovert inverted microscope in transmission using a halogen white light source *via* Zeiss EC Epiplan Apochromat 50x objective (numerical aperture (NA) = 0.95) forming a wide-field collection area diameter of 10 µm. Light transmitted *via* the sample was split with a beam splitter, with one component directed to a CCD camera (DCC3240C, Thorlabs) and the other coupled to a UV 600 nm optical fibre (200-800 nm spectral range) connected to a spectrometer (Avaspec-HS2048, Avantes).

Steady state PL microscopy

PL microscopy was performed using a Renishaw Invia confocal setup equipped with motorized piezo stage. Laser excitation was from an air-cooled Ar-ion (Argon ion) 514.5 nm continuous wave (CW) laser *via* 50x objective (NA = 0.75). The sample was excited upside down to ensure that the monolayer was excited first *via* the thin substrate to avoid shadowing by the QDs once deposited. Signals were collected in reflection *via* notch filter. The diffraction limited beam spot size was estimated as 0.84 µm. PL signal was dispersed *via* 600 l/mm grating prior to detection with inbuilt CCD detector. Laser power was measured directly *via* 5x objective with a Thorlabs S130C photodiode and PM100D power meter.

The detection wavelength range for PL measurements were selected using the setup's inbuilt WIRE software. The Vis-NIR PL spectrum (Figure 1.b) was generated with 10 s integration at a single spot on the heterostructure. The corresponding QD PL spectrum was taken at a location away from the heterostructure. The NIR PL map (Figure 2.a.) was generated with 8 µm resolution and 2 s integration. The Vis PL maps (Figure 5.a) was generated with 2 µm resolution and 0.5 s integration. All PL measurements were performed at 0.44 μW (80.2 W/cm^2).

Excitonic species were deconvoluted from pristine and heterostructure PL spectra using a procedure written in Matlab. The code incorporates the `gauss2' two Gaussian model fit. Further information on the Gaussian model is available *via* the *mathsworks* website.

Photoluminescence Excitation microscopy

PLE measurements were performed using a custom built inverted PL microscope setup. The inverted microscope arrangement enabled excitation of WS_2 monolayer first *via* the thin glass slide hence avoiding shadowing by the QDs. Variable wavelength excitation was provided by a pulsed super continuum white light source (Fianium Whitelase) *via* a Bentham TMc 300 monochromator. The optical image of the heterostructure was acquired using 600 nm laser light at low power *via* 60x oil objective, producing a 200 µm circular wide field image on an EMCCD camera (Photometrics QuantEM^{TM} 512SC). A QD PL image of the heterostructure was obtained by filtering out the excitation wavelengths using a combination of 750 nm and 800 nm long pass filters. Further precaution was taken to remove any long wave component in the excitation line using a 750 nm short pass filter. An example of the QD PL image is given in SI figure 6, which was recorded using 620 nm excitation at 10 MHz pulse rate (~0.006 µJ/cm^2 fluence) and 20 s integration time. The region of interest was isolated by closing an iris in the detection line just before the camera.

The procedure for obtaining PLE spectra are as follows: i) The laser excitation *via* the monochromator was swept between the visible and NIR range. Given that the optics in the system were optimized for 600 nm and above, excitation was varied between 580 nm and 710 nm with 2 nm resolution. Each excitation was integrated for 20 s using 10 MHz pulses; ii) the wide field PL signal at each excitation was recorded, producing a spectrum of raw PL signal as a function of excitation wavelength; iii) the background signal was obtained by covering the detector and repeating i)-ii). The excitation power was recorded simultaneously using a Thorlabs S130C photodiode placed in the excitation line just before the sample, and a PM100D power meter interfaced with the data logging software and; iv) raw data was post-processed in *Origin* where the background spectrum was subtracted from the raw PL spectrum and normalised by the number of photons injected at each wavelength. Finally, the PLE spectrum was corrected with a system calibration file based on the PLE and absorption spectra of a high PLQE NIR dye.

Time Resolved PL microscopy

TRPL measurements were performed using a PicoQuant Microtime 200 inverted confocal setup. Excitation was provided using 509 nm pulsed laser excitation *via* an inverted 20x air objective (NA = 0.4), with estimated diffraction limited spot size of 1.55 µm. Signals were detected with a single photon avalanche diode (SPAD).

For WS_2 monolayer PL decay, the repetition rate was set to 20 MHz with 25 ps resolution to obtain PL decay data. Laser excitation was filtered out with a 510 nm long pass, and the NIR region of both

pristine and heterostructure PL were filtered out using a 700 nm short pass filter, allowing for collection of WS_2 PL only. All signals were scaled up to 1500 s, which was used on the lowest fluence measurement in the fluence series. Power was measured using an inbuilt photodetector at each fluence, which was previously calibrated in the same experimental conditions using a standard external power-meter. Care was taken to ensure that measurements were made on the same spot on the monolayer before and after QD deposition. The instrument response function was measured with a blank glass cover slide as used for the sample. Decay rates were fitted using a model developed in Origin, which consists of a Gaussian (as the IRF) convoluted with a double exponential decay.

For PbS-CdS PL decay, excitation was provided using the 509 nm pulsed laser at 0.5 MHz repetition rate and 200 ps resolution. The excitation signal was filtered out using a 510 nm long pass filter and QD emission was isolated with an 800 nm long pass filter, removing any signal from the underlying WS_2.

Figure 1.b inset: Heterostructure image

WS_2 nanocrystal graphics were developed in VESTA software[54] and parsed into ChemDraw3D (Perkin Elmer) for rendering. QD graphics were modelled using Blender 3D modelling software.

Acknowledgments

This project has received funding from the European Research Council (ERC) under the European Union's Horizon 2020 research and innovation programme (grant agreement No 758826 and 756962). The authors thank the Winton program for physics of sustainability for financial support. We also acknowledge funding from EPSRC grants EP/P027741/1, EP/M006360/1, EP/R023980/1, EP/L015978/1, EP/L016087/1, EP/P027741/1 and EP/P005152/1. S.D.S acknowledges support from the Royal Society and Tata Group (UF150033). GD acknowledges the Royal Society for funding through a Newton International Fellowship.

Author contributions

A.O.A.T fabricated and measured the samples, performed PL and PLE measurements, analysed and processed all data, produced graphs, produced heterostructure 3D illustration in TOC and wrote the paper. N.G. built the PLE setup. G.D. and A.B. performed time resolved PL measurements under the supervision of S.D.S. J.X. prepared the QDs. R.P. assisted in PL data analysis. J.S assisted in PLE data analysis. C.A.W performed WS_2 steady state absorption measurements. J.A. assisted in TRPL fitting. Z.L offered guidance use of VESTA software. A.R conceived and directed the research. All authors have contributed to the writing of the manuscript.

Supporting Information

Supporting Information (SI) Available: further information on photoluminescence excitation (PLE) data normalisation; details on photoluminescence contribution (PL_{ctr}) derivation; PLE study on heterostructures with alternative quantum dot to two-dimensional material (QD-2D) surface attachment ligands; detail on theoretical Förster resonance energy transfer (FRET) radius estimation; optical image of region in which PL data in Figure 5.a was obtained; energy transfer efficiency (equation 2) derivation and; wide-field quantum dot (QD) PL image on tungsten disulphide (WS_2) monolayer. This material is available free of charge *via* the internet at http://pubs.acs.org.

Data Availability

The data underlying all figures in the main text and supplementary information are available at the University of Cambridge data repository at https://doi.org/10.17863/CAM.58224

References

(1) Geim, A. K.; Novoselov, K. S. The Rise of Graphene. *Nat. Mater.* **2007**, *6*, 183–191. https://doi.org/10.1038/nmat1849.

(2) Zhang, X.; Zhang, S.; Chang, C.; Feng, Y.; Li, Y.; Dong, N.; Wang, K.; Zhang, L.; Blau, W. J.; Wang, J. Facile Fabrication of Wafer-Scale MoS_2 Neat Films with Enhanced Third-Order Nonlinear Optical Performance. *Nanoscale* **2015**, *7*, 2978–2986. https://doi.org/10.1039/C4NR07164F.

(3) Nicolosi, V.; Chhowalla, M.; Kanatzidis, M. G.; Strano, M. S.; Coleman, J. N. Liquid Exfoliation of Layered Materials. *Science.* **2013**, *340* , 1226419. https://doi.org/10.1126/science.1226419.

(4) Mak, K. F.; Lee, C.; Hone, J.; Shan, J.; Heinz, T. F. Atomically Thin MoS_2: A New Direct-Gap Semiconductor. *Phys. Rev. Lett.* **2010**, *105*, 136805.

(5) Mak, K. F.; Shan, J. Photonics and Optoelectronics of 2D Semiconductor Transition Metal Dichalcogenides. *Nat. Photonics* **2016**, *10*, 216–226. https://doi.org/10.1038/nphoton.2015.282.

(6) Liu, H.-L.; Shen, C.-C.; Su, S.-H.; Hsu, C.-L.; Li, M.-Y.; Li, L.-J. Optical Properties of Monolayer Transition Metal Dichalcogenides Probed by Spectroscopic Ellipsometry. *Appl. Phys. Lett.* **2014**, *105*, 201905. https://doi.org/10.1063/1.4901836.

(7) Kang, K.; Xie, S.; Huang, L.; Han, Y.; Huang, P. Y.; Mak, K. F.; Kim, C. J.; Muller, D.; Park, J. High-Mobility Three-Atom-Thick Semiconducting Films with Wafer-Scale Homogeneity. *Nature* **2015**, *520*, 656–660. https://doi.org/10.1038/nature14417.

(8) Briggs, N.; Subramanian, S.; Lin, Z.; Li, X.; Zhang, X.; Zhang, K.; Xiao, K.; Geohegan, D.; Wallace, R.; Chen, L. Q.; Terrones, M.; Ebrahimi, A.; Das, S.; Redwing, J.; Hinkle, C.; Momeni, K.; van Duin, A.; Crespi, V.; Kar, S.; Robinson, J. A . A Roadmap for Electronic Grade 2D Materials. *2D Mater.* **2019**, *6*. https://doi.org/10.1088/2053-1583/aaf836.

(9) Amani, M.; Lien, D. H.; Kiriya, D.; Xiao, J.; Azcatl, A.; Noh, J.; Madhvapathy, S. R.; Addou, R.; Santosh, K. C.; Dubey, M.; Cho, K.; Wallace, R. M.; Lee, S.-C.; He, J.-H.; Ager, J. W.; Zhang, X.; Yablonovitch, E.; Javey, A . Near-Unity Photoluminescence Quantum Yield in MoS_2. *Science.* **2015**, *350*, 1065–1068. https://doi.org/10.1126/science.aad2114.

(10) Kim, H.; Lien, D. H.; Amani, M.; Ager, J. W.; Javey, A. Highly Stable near-Unity Photoluminescence Yield in Monolayer MoS_2 by Fluoropolymer Encapsulation and Superacid Treatment. *ACS Nano* **2017**, *11*, 5179–5185. https://doi.org/10.1021/acsnano.7b02521.

(11) Tanoh, A. O. A.; Alexander-Webber, J.; Xiao, J.; Delport, G.; Williams, C. A.; Bretscher, H.; Gauriot, N.; Allardice, J.; Pandya, R.; Fan, Y.; Fan, Y.; Li, Z.; Vignolini, S.; Stranks, S. D.; Hofmann, S.; Rao, A. Enhancing Photoluminescence and Mobilities in WS_2 Monolayers with Oleic Acid Ligands. *Nano Lett.* **2019**, *19*, 6299–6307. https://doi.org/10.1021/acs.nanolett.9b02431.

(12) Wang, Q.; Kalantar-Zadeh, K.; Kis, A.; Coleman, J. N.; Strano, M. S. Electronics and Optoelectronics of Two-Dimensional Transition Metal Dichalcogenides. *Nat. Nanotechnol.* **2012**, *7*, 699–712. https://doi.org/10.1038/nnano.2012.193.

(13) Berkelbach, T. C.; Hybertsen, M. S.; Reichman, D. R. Theory of Neutral and Charged Excitons in Monolayer Transition Metal Dichalcogenides. *Phys. Rev. B - Condens. Matter Mater. Phys.*

2013, *88*, 045318. https://doi.org/10.1103/PhysRevB.88.045318.

(14) Ye, Z.; Cao, T.; O'Brien, K.; Zhu, H.; Yin, X.; Wang, Y.; Louie, S. G.; Zhang, X. Probing Excitonic Dark States in Single-Layer Tungsten Disulphide. *Nature* **2014**, *513*, 214–218. https://doi.org/10.1038/nature13734.

(15) Berkelbach, T. C.; Reichman, D. R. Optical and Excitonic Properties of Atomically Thin Transition-Metal Dichalcogenides. *Annu. Rev. Condens. Matter Phys.* **2018**, *9*, annurev-conmatphys-033117-054009. https://doi.org/10.1146/annurev-conmatphys-033117-054009.

(16) Barbone, M.; Montblanch, A. R. P.; Kara, D. M.; Palacios-Berraquero, C.; Cadore, A. R.; De Fazio, D.; Pingault, B.; Mostaani, E.; Li, H.; Chen, B.; Watanabe, K.; Taniguchi, T.; Tongay, S.; Wang, G.; Ferrari, A.C.; Atatüre, M. Charge-Tuneable Biexciton Complexes in Monolayer WSe_2. *Nat. Commun.* **2018**, *9*, 3721. https://doi.org/10.1038/s41467-018-05632-4.

(17) Chernikov, A.; Berkelbach, T. C.; Hill, H. M.; Rigosi, A.; Li, Y.; Aslan, O. B.; Reichman, D. R.; Hybertsen, M. S.; Heinz, T. F. Exciton Binding Energy and Nonhydrogenic Rydberg Series in Monolayer WS_2. *Phys. Rev. Lett.* **2014**, *113*, 076802. https://doi.org/10.1103/PhysRevLett.113.076802.

(18) Alivisatos, A. P. Semiconductor Clusters, Nanocrystals, and Quantum Dots. *Science.* **1996**, *271* (5251), 933–937.

(19) Achermann, M.; Petruska, M. A.; Kos, S.; Smith, D. L.; Koleske, D. D.; Klimov, V. I. Energy-Transfer Pumping of Semiconductor Nanocrystals Using an Epitaxial Quantum Well. *Nature* **2004**, *429*, 642–646. https://doi.org/10.1038/nature02571.

(20) Förster, T. Transfer Mechanisms of Electronic Excitation. *Discuss. Faraday Soc.* **1959**, *27*, 7–17.

(21) Guzelturk, B.; Demir, H. V. Near-Field Energy Transfer Using Nanoemitters For Optoelectronics. *Adv. Funct. Mater.* **2016**, *26*, 8158–8177. https://doi.org/10.1002/adfm.201603311.

(22) Prasai, D.; Klots, A. R.; Newaz, A.; Niezgoda, J. S.; Orfield, N. J.; Escobar, C. A.; Wynn, A.; Efimov, A.; Jennings, G. K.; Rosenthal, S. J.; Bolotin, K.I. Electrical Control of near-Field Energy Transfer between Quantum Dots and Two-Dimensional Semiconductors. *Nano Lett.* **2015**, *15*, 4374–4380. https://doi.org/10.1021/acs.nanolett.5b00514.

(23) Wu, L.; Chen, Y.; Zhou, H.; Zhu, H. Ultrafast Energy Transfer of Both Bright and Dark Excitons in 2D van der Waals Heterostructures beyond Dipolar Coupling. *ACS Nano* **2019**, *13*, 2341–2348. https://doi.org/10.1021/acsnano.8b09059.

(24) Boulesbaa, A.; Wang, K.; Mahjouri-Samani, M.; Tian, M.; Puretzky, A. A.; Ivanov, I.; Rouleau, C. M.; Xiao, K.; Sumpter, B. G.; Geohegan, D. B. Ultrafast Charge Transfer and Hybrid Exciton Formation in 2D/0D Heterostructures. *J. Am. Chem. Soc.* **2016**, *138*, 14713–14719. https://doi.org/10.1021/jacs.6b08883.

(25) Kufer, D.; Nikitskiy, I.; Lasanta, T.; Navickaite, G.; Koppens, F. H. L.; Konstantatos, G. Hybrid 2D-0D MoS_2-PbS Quantum Dot Photodetectors. *Adv. Mater.* **2015**, *27*, 176–180. https://doi.org/10.1002/adma.201402471.

(26) Huang, Y.; Zhuge, F.; Hou, J.; Lv, L.; Luo, P.; Zhou, N.; Gan, L.; Zhai, T. van der Waals Coupled Organic Molecules with Monolayer MoS_2 for Fast Response Photodetectors with Gate-Tunable Responsivity. *ACS Nano* **2018**, *12*, 4062–4073. https://doi.org/10.1021/acsnano.8b02380.

(27) Huo, N.; Gupta, S.; Konstantatos, G. MoS_2–HgTe Quantum Dot Hybrid Photodetectors beyond 2 μm. *Adv. Mater.* **2017**, *29*, 1606576. https://doi.org/10.1002/adma.201606576.

(28) Nazir, G.; Khan, M. F.; Akhtar, I.; Akbar, K.; Gautam, P.; Noh, H.; Seo, Y.; Chun, S. H.; Eom, J.

Enhanced Photoresponse of ZnO Quantum Dot-Decorated MoS_2 Thin Films. *RSC Adv.* **2017**, *7*, 16890–16900. https://doi.org/10.1039/c7ra01222e.

(29) Wu, H.; Si, H.; Zhang, Z.; Kang, Z.; Wu, P.; Zhou, L.; Zhang, S.; Zhang, Z.; Liao, Q.; Zhang, Y. All-Inorganic Perovskite Quantum Dot-Monolayer MoS_2 Mixed-Dimensional van der Waals Heterostructure for Ultrasensitive Photodetector. *Adv. Sci.* **2018**, *5*, 1801219. https://doi.org/10.1002/advs.201801219.

(30) Li, M.; Chen, J. S.; Routh, P. K.; Zahl, P.; Nam, C. Y.; Cotlet, M. Distinct Optoelectronic Signatures for Charge Transfer and Energy Transfer in Quantum Dot–MoS_2 Hybrid Photodetectors Revealed by Photocurrent Imaging Microscopy. *Adv. Funct. Mater.* **2018**, *28*, 1707558. https://doi.org/10.1002/adfm.201707558.

(31) Kang, D. H.; Pae, S. R.; Shim, J.; Yoo, G.; Jeon, J.; Leem, J. W.; Yu, J. S.; Lee, S.; Shin, B.; Park, J. H. An Ultrahigh-Performance Photodetector Based on a Perovskite–Transition-Metal-Dichalcogenide Hybrid Structure. *Adv. Mater.* **2016**, *28*, 7799–7806. https://doi.org/10.1002/adma.201600992.

(32) Yu, Y.; Zhang, Y.; Song, X.; Zhang, H.; Cao, M.; Che, Y.; Dai, H.; Yang, J.; Zhang, H.; Yao, J. PbS-Decorated WS_2 Phototransistors with Fast Response. *ACS Photonics* **2017**, *4*, 950–956. https://doi.org/10.1021/acsphotonics.6b01049.

(33) Hu, C.; Dong, D.; Yang, X.; Qiao, K.; Yang, D.; Deng, H.; Yuan, S.; Khan, J.; Lan, Y.; Song, H.; Tang, J. Synergistic Effect of Hybrid PbS Quantum Dots/2D-WSe_2 toward High Performance and Broadband Phototransistors. *Adv. Funct. Mater.* **2017**, *27*, 1603605. https://doi.org/10.1002/adfm.201603605.

(34) Prins, F.; Goodman, A. J.; Tisdale, W. A. Reduced Dielectric Screening and Enhanced Energy Transfer in Single- and Few-Layer MoS_2. *Nano Lett.* **2014**, *14*, 6087–6091. https://doi.org/10.1021/nl5019386.

(35) Raja, A.; Montoya−Castillo, A.; Zultak, J.; Zhang, X.-X.; Ye, Z.; Roquelet, C.; Chenet, D. A.; van der Zande, A. M.; Huang, P.; Jockusch, S.; Hone, J.; Reichman, D. R.; Brus, L.E.; Heinz, T. F. Energy Transfer from Quantum Dots to Graphene and MoS_2 : The Role of Absorption and Screening in Two-Dimensional Materials. *Nano Lett.* **2016**, *16*, 2328–2333. https://doi.org/10.1021/acs.nanolett.5b05012.

(36) Zang, H.; Routh, P. K.; Huang, Y.; Chen, J.-S.; Sutter, E.; Sutter, P.; Cotlet, M. Nonradiative Energy Transfer from Individual CdSe/ZnS Quantum Dots to Single-Layer and Few-Layer Tin Disulfide. *ACS Nano* **2016**, *10*, 4790–4796. https://doi.org/10.1021/acsnano.6b01538.

(37) Liu, H.; Wang, T.; Wang, C.; Liu, D.; Luo, J. Exciton Radiative Recombination Dynamics and Nonradiative Energy Transfer in Two-Dimensional Transition-Metal Dichalcogenides. *J. Phys. Chem. C* **2019**, *123*, 10087–10093. https://doi.org/10.1021/acs.jpcc.8b12179.

(38) Liu, Y.; Li, H.; Zheng, X.; Cheng, X.; Jiang, T. Giant Photoluminescence Enhancement in Monolayer WS_2 by Energy Transfer from $CsPbBr_3$ Quantum Dots. *Opt. Mater. Express* **2017**, *7*, 1327. https://doi.org/10.1364/ome.7.001327.

(39) Li, H.; Zheng, X.; Liu, Y.; Zhang, Z.; Jiang, T. Ultrafast Interfacial Energy Transfer and Interlayer Excitons in the Monolayer WS2/CsPbBr3 Quantum Dot Heterostructure. *Nanoscale* **2018**, *10*, 1650–1659. https://doi.org/10.1039/c7nr05542k.

(40) Ehrler, B.; Walker, B. J.; Böhm, M. L.; Wilson, M. W. B.; Vaynzof, Y.; Friend, R. H.; Greenham, N. C. *In Situ* Measurement of Exciton Energy in Hybrid Singlet-Fission Solar Cells. *Nat. Commun.* **2012**, *3*. https://doi.org/10.1038/ncomms2012.

(41) Tabachnyk, M.; Ehrler, B.; Gélinas, S.; Böhm, M. L.; Walker, B. J.; Musselman, K. P.; Greenham, N. C.; Friend, R. H.; Rao, A. Resonant Energy Transfer of Triplet Excitons from Pentacene to PbSe Nanocrystals. *Nat. Mater.* **2014**, *13*, 1033–1038. https://doi.org/10.1038/NMAT4093.

(42) Amani, M.; Taheri, P.; Addou, R.; Ahn, G. H.; Kiriya, D.; Lien, D. H.; Ager, J. W.; Wallace, R. M.; Javey, A. Recombination Kinetics and Effects of Superacid Treatment in Sulfur- and Selenium-Based Transition Metal Dichalcogenides. *Nano Lett.* **2016**, *16*, 2786–2791. https://doi.org/10.1021/acs.nanolett.6b00536.

(43) Cademartiri, L.; Montanari, E.; Calestani, G.; Migliori, A.; Guagliardi, A.; Ozin, G. A. Size-Dependent Extinction Coefficients of PbS Quantum Dots. *J. Am. Chem. Soc.* **2006**, *128*, 10337–10346. https://doi.org/10.1021/ja063166u.

(44) Del Valle, J. C.; Catalán, J. Kasha's Rule: A Reappraisal. *Phys. Chem. Chem. Phys.* **2019**, *21*, 10061–10069. https://doi.org/10.1039/c9cp00739c.

(45) Xu, F.; Gerlein, L. F.; Ma, X.; Haughn, C. R.; Doty, M. F.; Cloutier, S. G. Impact of Different Surface Ligands on the Optical Properties of PbS Quantum Dot Solids. *Materials (Basel).* **2015**, *8*, 1858–1870. https://doi.org/10.3390/ma8041858.

(46) Huang, Z.; Xu, Z.; Mahboub, M.; Li, X.; Taylor, J. W.; Harman, W. H.; Lian, T.; Tang, M. L. PbS/CdS Core–Shell Quantum Dots Suppress Charge Transfer and Enhance Triplet Transfer. *Angew. Chem. Int. Ed.* **2017**, *56*, 16583–16587. https://doi.org/10.1002/anie.201710224.

(47) Goodman, A. J.; Willard, A. P.; Tisdale, W. A. Exciton Trapping Is Responsible for the Long Apparent Lifetime in Acid-Treated MoS_2. *Phys. Rev. B* **2017**, *96*, 121404(R). https://doi.org/10.1103/PhysRevB.96.121404.

(48) Palummo, M.; Bernardi, M.; Grossman, J. C. Exciton Radiative Lifetimes in Two-Dimensional Transition Metal Dichalcogenides. *Nano Lett.* **2015**, *15*, 2794–2800. https://doi.org/10.1021/nl503799t.

(49) Wei, K.; Liu, Y.; Yang, H.; Cheng, X.; Jiang, T. Large Range Modification of Exciton Species in Monolayer WS_2. *Appl. Opt.* **2016**, *55*, 6251. https://doi.org/10.1364/AO.55.006251.

(50) Desai, S. B.; Madhvapathy, S. R.; Amani, M.; Kiriya, D.; Hettick, M.; Tosun, M.; Zhou, Y.; Dubey, M.; Ager, J. W.; Chrzan, D.; Javey, A . Gold-Mediated Exfoliation of Ultralarge Optoelectronically-Perfect Monolayers. *Adv. Mater.* **2016**, *28*, 4053–4058. https://doi.org/10.1002/adma.201506171.

(51) Li, H.; Wu, J.; Huang, X.; Lu, G.; Yang, J.; Lu, X.; Xiong, Q.; Zhang, H. Rapid and Reliable Thickness Identification of Two-Dimensional Nanosheets Using Optical Microscopy. *ACS Nano* **2013**, *7*, 10344–10353. https://doi.org/10.1021/nn4047474.

(52) Hines, M. A.; Scholes, G. D. Colloidal PbS Nanocrystals with Size-Tunable near-Infrared Emission: Observation of Post-Synthesis Self-Narrowing of the Particle Size Distribution. *Adv. Mater.* **2003**, *15*, 1844–1849. https://doi.org/10.1002/adma.200305395.

(53) Neo, M. S.; Venkatram, N.; Li, G. S.; Chin, W. S.; Ji, W. Synthesis of PbS/CdS Core-Shell QDs and Their Nonlinear Optical Properties. *J. Phys. Chem. C* **2010**, *114*, 18037–18044. https://doi.org/10.1021/jp104311j.

(54) Momma, K.; Izumi, F. VESTA 3 for Three-Dimensional Visualization of Crystal, Volumetric and Morphology Data. *J. Appl. Crystallogr.* **2011**, *44*, 1272–1276. https://doi.org/10.1107/S0021889811038970.

Figures

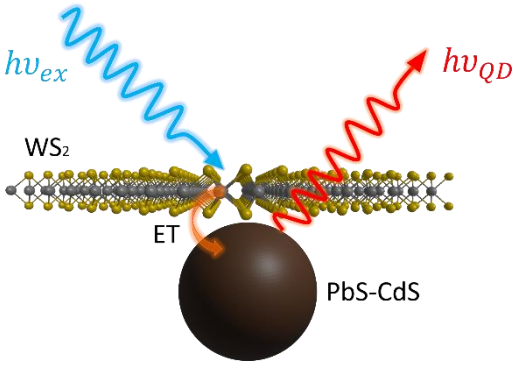

TOC

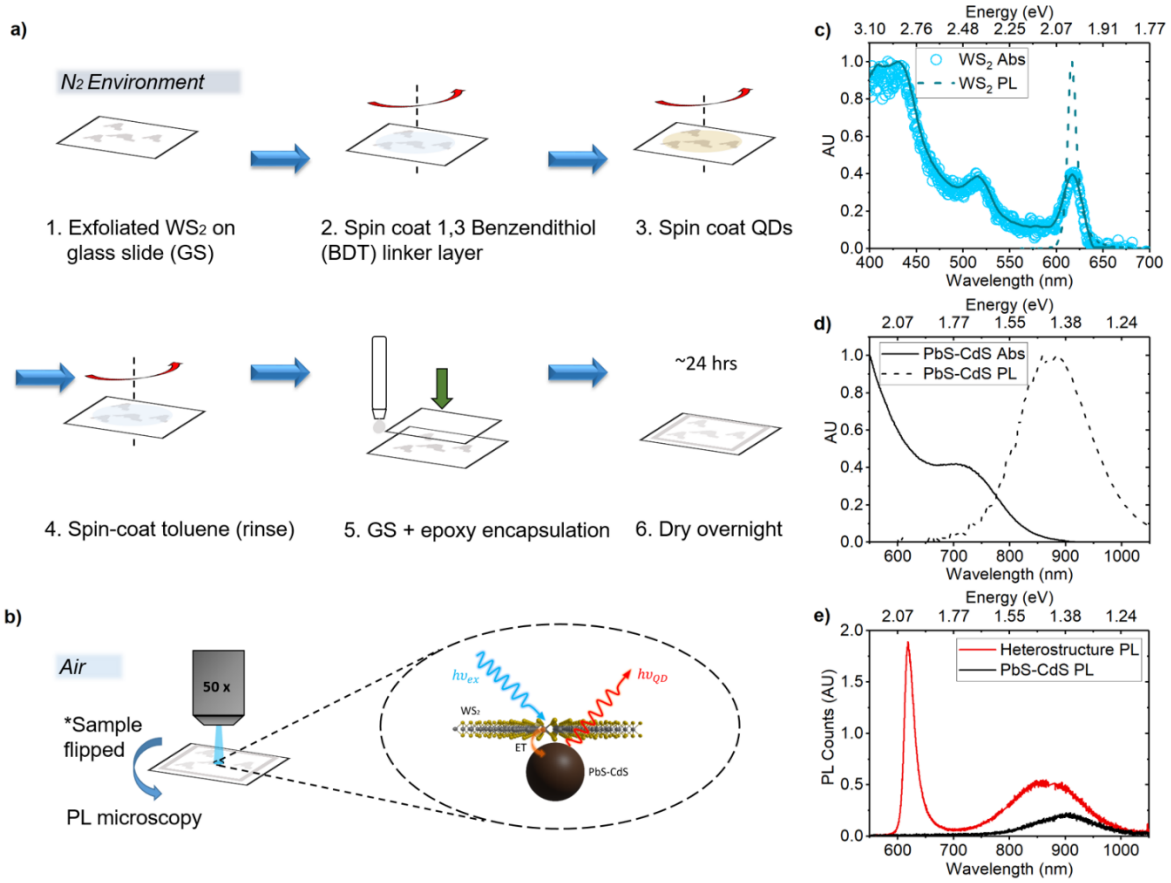

Fig 1 a-e: a) Cartoon illustrating heterostructure sample fabrication process (1-6) and **b)** initial PL characterization *via* 50x objective; **c)** Monolayer WS_2 normalised absorption (light blue circles with solid dark blue line as guide to eye) and PL (dashed dark blue line). **d)** Colloidal PbS-CdS normalised absorption (black solid line) and PL (black dashed line) spectra; **e)** PL spectra of WS_2-PbS-CdS 2D-QD heterostructure (red) and PbS-CdS film on bare glass substrate (black) measured with 514.5 nm CW laser at 80.2 W/cm^2.

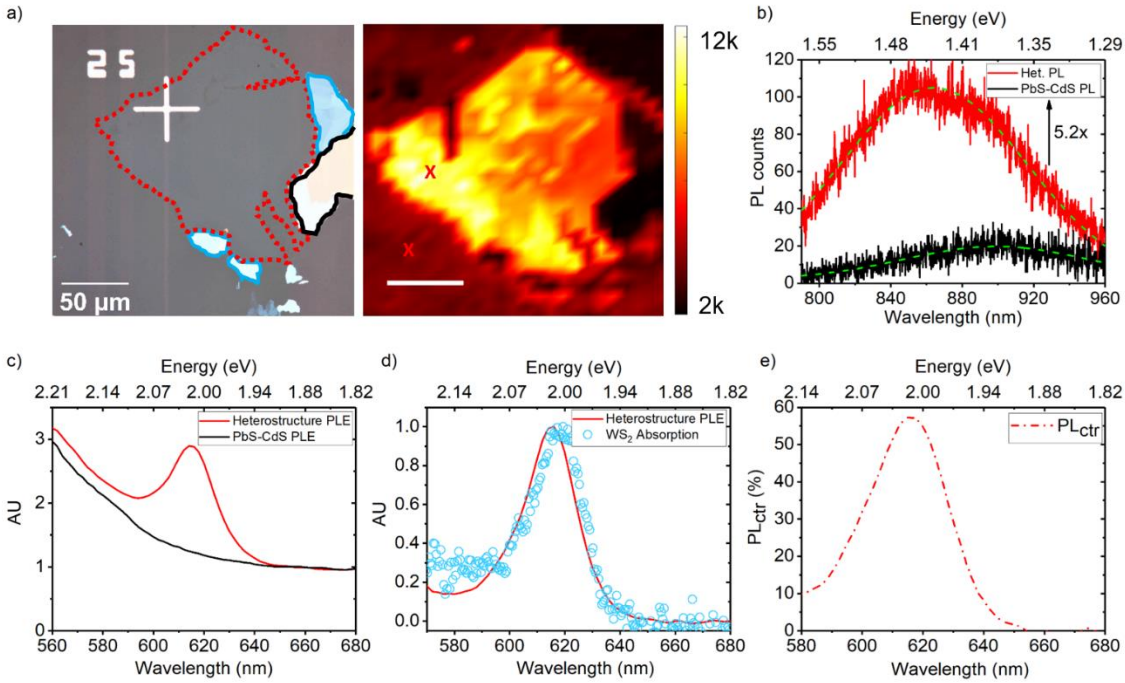

Fig 2 a-e: **a)** Optical micrograph of a WS_2 flake (left) showing monolayer (red dotted outline), multilayers (blue outline) and bulk crystal (black outline) with corresponding confocal NIR PL map of QD emission from the heterostructure (right) measured with 514.5 nm CW laser at 80.2 W/cm^2. RHS scale bar represents 50 µm; **b)** QD PL spectra from heterostructure (red) and bare substrate (black) taken from points marked `*x*' in Figure 2.a, RHS. Green dashed lined represent single Gaussian peak fits; **c)** Normalised PLE spectra of heterostructure (red) and QD (control) obtained *via* scanning wavelengths about the $WS_2$ `A' exciton (616 nm) and detecting QD PL (900 nm). PLE spectra normalised by the average signal between 670 nm and 700 nm; **d)** Normalised `subtract' (red) signal derived *via* subtraction of QD PLE signal from heterostructure PLE signal in Fig. 2.b and overlapped with typical WS_2 absorption spectrum (blue circles); **e)** Estimated contribution to QD PL (PL_{ctr}) by the WS_2 monolayer as a function of excitation wavelength with peak value of 58% at 616 nm (~2.0 eV).

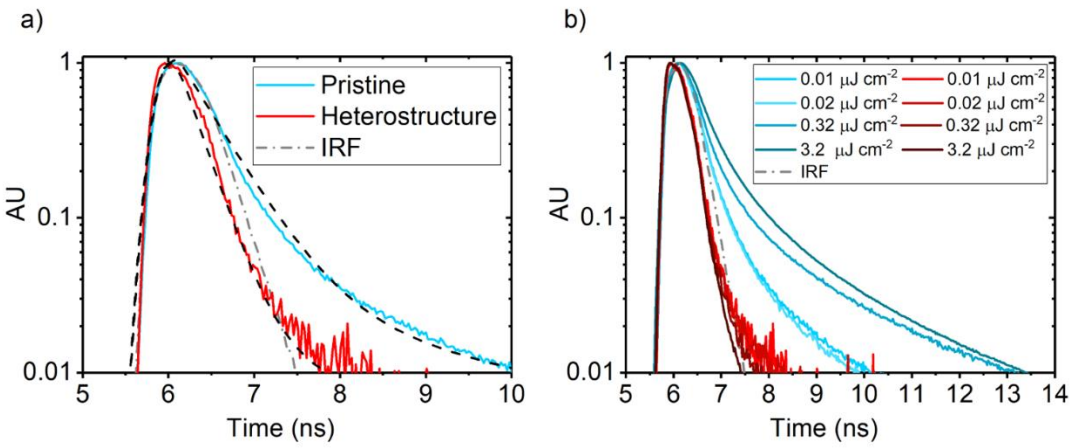

Fig 3 a-b: a) Low fluence time resolved WS_2 PL decay signals from pristine (blue) and heterostructure (red) samples measured with 509 nm pulsed excitation at 0.01 μJ/cm^2. Exponential decay fits are shown as dotted black lines; **b)** Time resolved WS_2 PL decay fluence series from pristine (blue) and heterostructure (red) samples. Pristine WS_2 PL decay signals show general increase in lifetime as a function of pump fluence due to exciton trapping. All WS_2 PL in heterostructure signal quenched below instrument response function (IRF) (grey dash-dot line) due to fast exciton transfer.

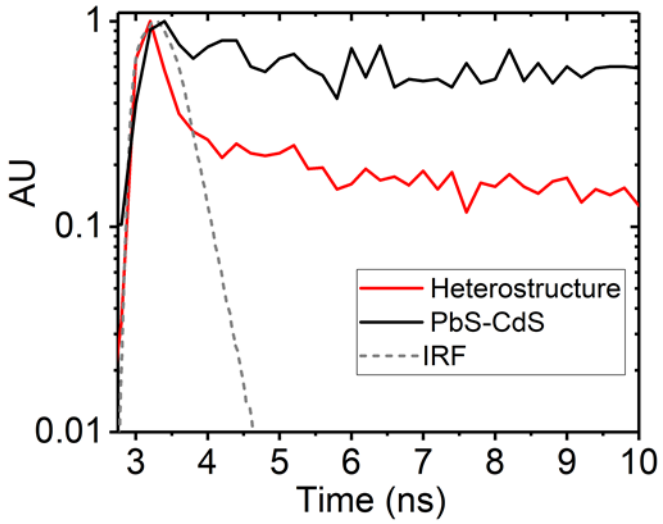

Fig 4: QD TRPL decay spectra of heterostructure (red) and bare substrate (black) measured with 509 nm pulsed excitation at 0.5 MHz. The early time signal in heterostructure PL decay convoluted with IRF confirms that ET phenomenon faster than resolution of TCSPC setup available for this study.

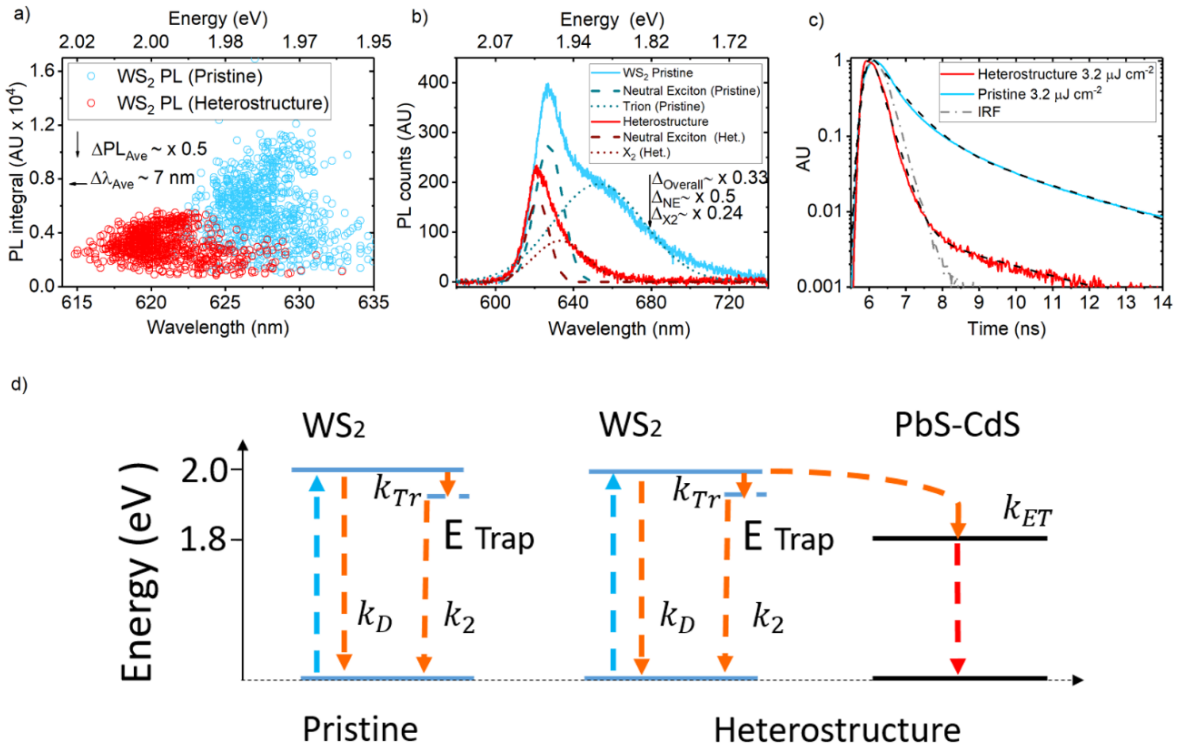

Fig 5 a-d: a) Scatter plots of monolayer WS_2 (visible) PL integrals and the corresponding PL peak wavelengths extracted from spatial PL maps of the sample in pristine (blue) and heterostructure (red) form. PL measured with 514 nm continuous wave (CW) laser excitation at 80.2 W cm^{-2} intensity; **b)** WS_2 PL spectra of an exemplary on the monolayer in pristine (blue) and heterostructure (red) cases. Spectra are deconvoluted with Gaussian peaks which represent the neutral exciton (dashed lines) and a lower energy species X_2 (dotted lines); **c)** TRPL decay spectra of pristine (blue) and heterostructure (red), measured with 509 nm excitation at 63.4 W cm^{-2} intensity. Black dashed lines represent decay fits. IRF given by grey dot-dash line; **d)** Energy level diagram illustrating radiative exciton pathways in pristine WS_2 (LHS) and in heterostructure. Blue arrows represent initial excitation, orange arrows represent WS_2 excitons and red arrows represent down-shifted excitons that recombine at lower energy in the PbS-CdS QD.

Supporting Information:

Directed Energy Transfer from Monolayer WS2 to near Infrared Emitting PbS-CdS Quantum Dots

Arelo O.A Tanoh[1,2], Nicolas Gauriot[1], Géraud Delport[1], James Xiao[1], Raj Pandya[1], Jooyoung Sung[1], Jesse Allardice[1], Zhaojun Li[1], Cyan A. Williams [2,3], Alan Baldwin[1], Samuel D. Stranks[1,4], Akshay Rao[1*]

[1]Cavendish Laboratory, Cambridge, JJ Thomson Avenue, CB3 0HE, Cambridge, United Kingdom

[2]Cambridge Graphene Centre, University of Cambridge, 9 JJ Thomson Avenue, Cambridge, CB3 0FA, Cambridge, United Kingdom

[3]Department of Chemistry, University of Cambridge, Lensfield Rd, CB2 1EW, Cambridge, United Kingdom

[4]Department of Chemical Engineering & Biotechnology Department of Chemical Engineering & Biotechnology, University of Cambridge, Philippa Fawcett Drive, Cambridge CB3 0AS, UK.

*E-mail: ar525@cam.ac.uk

Section 1: Photoluminescence excitation (PLE) data scaling

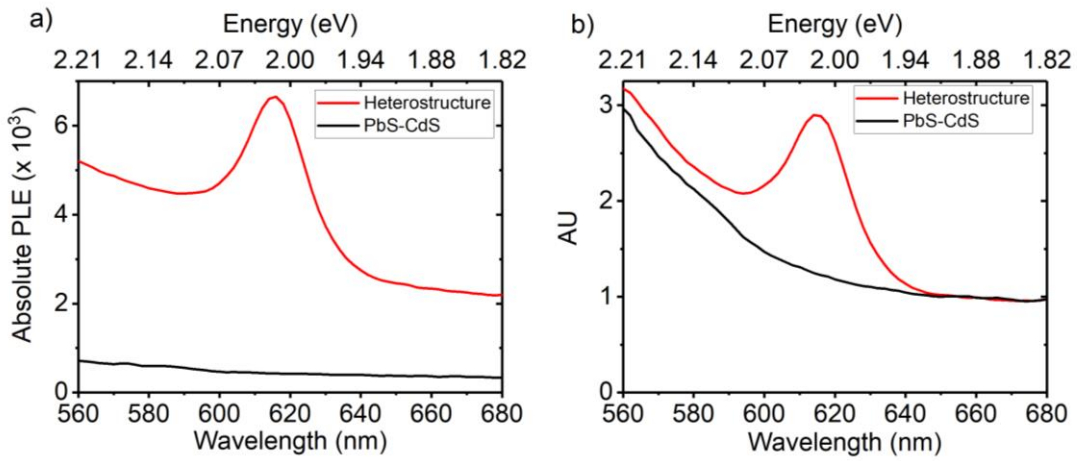

SI Figure 1 a-b: **a)** Unscaled heterostructure (red) and PbS-CdS (black) PLE data. **b)** Heterostructure and PbS-CdS PLE normalised to mean PLE values off-resonant to underlying WS_2 donor (670-700 nm).

Section 2: Photoluminescence contribution (PL_{ctr}) derivation

The photoluminescence contribution (PL_{ctr}) by the transition metal dichalcogenide (TMD) monolayer to the quantum dot (QD) emitter is derived. Vavilov's rule,[1] which states that PLQE is independent of excitation wavelength, forms the key assumption in this derivation. Given the range of wavelengths presented in PLE measurements (560 nm – 680 nm) this assumption is regarded as reasonable. We consider the photoluminescence excitation (PLE) of the QD at excitation resonant and non-resonant to the underlying WS_2 monolayer *i.e.* $PLE_{\lambda*}$ and PLE_{λ} respectively. In each case the PLE from the QD emission detection is given by *equations 1* and *2*:

$$PLE_{\lambda*} = \frac{PL_{\lambda*}}{n_{\lambda*}} = Abs_{\lambda*} \times PLQE \tag{1}$$

$$PLE_{\lambda} = \frac{PL_{\lambda}}{n_{\lambda}} = Abs_{\lambda} \times PLQE \tag{2}$$

Where *n* and *Abs* are the number of photons per second injected and absorption of the QDs. By dividing *equation 1* by *equation 2* we obtain:

$$\frac{PLE_{\lambda*}}{PLE_{\lambda}} = \left(\frac{n_{\lambda}}{n_{\lambda*}}\right)\frac{PL_{\lambda*}}{PL_{\lambda}} = \left(\frac{Abs_{\lambda*}}{Abs_{\lambda}}\right) \tag{3}$$

Hence the absorption ratio is equivalent to the ratio of WS_2 resonant PLE to non-resonant PLE. This is ratio is given by *R*:

$$R = \frac{PLE_{\lambda*}}{PLE_{\lambda}} = \left(\frac{n_{\lambda}}{n_{\lambda*}}\right)\frac{PL_{\lambda*}}{PL_{\lambda}} = \left(\frac{Abs_{\lambda*}}{Abs_{\lambda}}\right) \tag{4}$$

By comparing the *R* values on the heterostructure and the QD control, we can identify an additional contribution to the QD absorption *i.e.* ΔR from the underlying WS_2.

$$\Delta R = R_{Het} - R_{QD} \tag{5}$$

Expressing equation (6) as a proportion of the heterostructure R value (R_{Het}), we obtain the contribution of PL by the WS_2 to the QDs.

$$PL_{ctr} = \left(\frac{R_{Het} - R_{QD}}{R_{Het}}\right) = \left(\frac{\Delta R}{R_{Het}}\right) \tag{6}$$

Section 3: Corroborating Förster resonance energy transfer (FRET)

Section 3.1: PLE study on heterostructures with alternative quantum dot to two dimensional material (QD-2D) surface attachment ligands of increasing length

SI figure 2 shows the wide field PLE spectra of tungsten disulphide/ lead sulphide-cadmium sulphide (WS_2/PbS-CdS) heterostructures with varying QD-2D surface attachment thiol ligands. Table 1 lists the ligands used and their corresponding lengths. The difference in prominence of the WS_2 resonant peak is due to the variation in size of the WS_2 monolayers used. The 1,3 Benzene dithiol (BDT) sample has the largest monolayer and hence the most prominent WS_2 `A' exciton signal with less contribution of the QD emission shoulder blue of the $WS_2$ peak as seen in other samples. All signals were obtained by scanning about $WS_2$ `A' exciton and detecting and PbS-CdS emission (~ 900 nm). All signals show the WS_2 `A' exciton peak in the expected spectral region (614 – 620 nm).

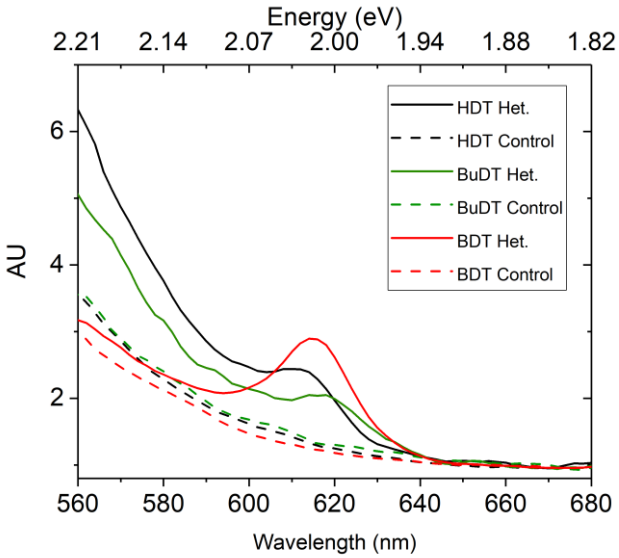

SI Fig 2: Normalised PLE spectra of 2D-QD heterostructures with varying surface ligands, namely BDT (red), Butane dithiol (BuDT) (green) and Hexane dithiol (HDT)(black). Dashed lines represent control signals.

Table 1: Dithiol ligands and corresponding lengths. *(*)* indicates value estimated using calculated dithiol ligand lengths from the open literature (Mispelon *et al.*,[2] Table 1, p. 18566) and the known bond angle of a hexagonal planar benzene ring

Ligand	Length	Reference
1,3 Benzene dithiol (BDT)	0.47 nm	*
1,4 Butane dithiol (BuDT)	0.68 nm	[3]
1,6 Hexane dithiol (HDT)	0.95 nm	[3]

While charge orbital overlap between donor and acceptor species is a possibility at these separation distances, the high oscillator strengths of the TMD donor and QD acceptor still render ET *via* dipole interaction (*i.e*. FRET) highly favourable,[4] and more significant than proximity dependent Dexter energy transfer (DET).

The Förster radius, R_0, is defined as the distance between donor and acceptor through which there is a 50% probability excitation transfer.[5] we therefore estimate the theoretical Förster radius to quantify the likelihood of FRET being the dominant ET mechanism from 2D → QD in the heterostructures measured.

Section 3.2: Theoretical FRET radius estimation

Considering the 2D TMD as an array of point-like emitters and the QD film as an array of point-like absorbers, the FRET radius, R_0, is defined in equation 7.[4] This system is also well approximated by a 2D quantum well donor and nanoparticle acceptors, which follows a d^{-6} distance dependence for non-radiative energy transfer.[6]

$$R_0^6 = \frac{9ln10}{128\pi^5 N_A}\frac{\kappa^2 PLQE_D}{n^4}J \quad (7)$$

N_A is Avogadro's number, n is the refractive index of the medium surrounding the FRET pair, $PLQE_D$ is the donor's intrinsic photoluminescence quantum efficiency and κ^2 is the dipole orientation factor, which is equal to 2/3 for randomly oriented dipoles.[7] J is the overlap integral between the area normalised emission spectrum,[4] F_D and acceptor absorption spectrum given by the acceptor molar extinction coefficient, ε_A.

$$J = \int_0^\infty F_D(\lambda)\varepsilon_A(\lambda)\lambda^4\, d\lambda \quad (8)$$

It must be noted that J is evaluated with the wavelength in [nm] and ε_A in [M^{-1} cm^{-1}]. To compute R_0, we must calculate the overlap integral J from measured $\varepsilon_A(\lambda)$ and $F_D(\lambda)$ data. The molar extinction coefficient is obtained *via* Beer Lambert's law (*equation 9*) for absorbance, A of a 0.1 mg ml^{-1} suspension of QDs in toluene of molar concentration c, measured with a 1 cm path length, l, cuvette.

$$A(\lambda) = \varepsilon_A(\lambda)cl \quad (9)$$

However, to obtain the molar extinction coefficient, the molar concentration, c of QDs in [M] is needed. The first step in calculating c involves estimating the QD size by solving *equation 10* provided by Moreels *et al.*[8] for PbS QDs of diameter D using their band gap energy, E_O. Since the QDs used consist mainly of a PbS core as per the modified preparation method originally developed by Neo *et al.*,[9] the use of equation 10 is considered reasonable. For the QDs used, where E_O ~1.76 eV, we get D ~ 2.4 nm.

$$E_0 = 0.41 + \frac{1}{0.0252D^2 + 0.283D} \quad (10)$$

We then calculate the QD volume assuming a spherical shape. This is followed by multiplying the volume by the density of PbS (7.6 g cm^{-3}) to obtain the mass of a single QD. Multiplying the mass of a single QD by the Avogadro number yields an estimate for the QD molar mass, Mr ~ 33128 g mol^{-1}. Dividing the known QD concentration of 0.1 g L^{-1} (ie 0.1 mg mL^{-1}) by the estimated QD molar mass Mr, yields c ~ 3.02×10^{-6} M. We rearrange *equation 8* for molar extinction coefficient in [M^{-1} cm^{-1}], which is shown in SI figure 3 along with area normalised donor emission, F_D.

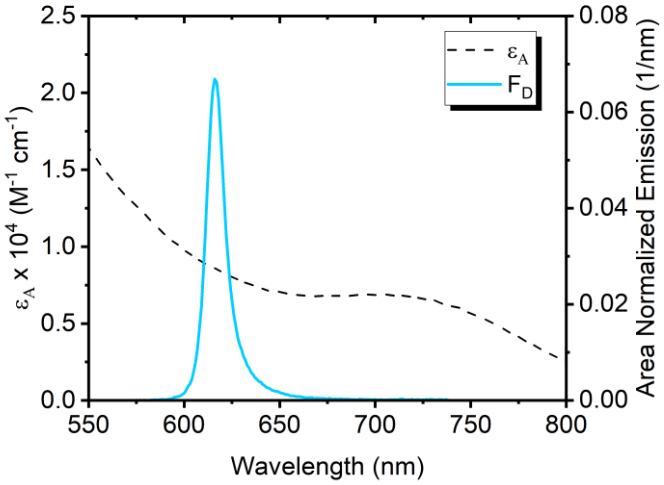

SI Fig 3: (Left axis) Molar extinction coefficient of 3.02×10^{-6} M PbS-CdS QDs in toluene measured with 1 cm cuvette. (Right axis) Area normalized WS_2 emission spectrum, F_D used to calculate overlap integral, J.

From the data shown in SI figure 3, the overlap integral is estimated *via equation 8* as $J \approx 1.23 \times 10^{15}$ M^{-1} cm^{-1} nm^4. Using a simplified version of *equation 7* below (*equation 11*) we estimate R_0 [nm] by assuming a vacuum between the emitter and absorber, *i.e.* $n = 1$ and orientation factor $\kappa^2 = 2/3$. For the ideal system, we assume the TMD donor to have unity PLQE. This approximation is however considered reasonable as we subsequently find that the energy transfer rate from WS_2 band edge to QD band edge outcompetes the intrinsic exciton quenching in WS_2, which is the known cause of low PLQE in newly prepared TMDs.

$$R_0 = 0.0211 \left(\frac{\kappa^2 PLQE_D}{n^4} J\right)^{\frac{1}{6}} \quad (11)$$

From *equation* 11, we obtain $\boldsymbol{R_0 \approx 6.5}$ **nm**, which exceeds the ligand separation distances between donor TMD and acceptor QD listed in table 1. This highlights the significance of the oscillator strength of the constituent heterostructure materials over their physical separation distance. This strongly implies FRET as the dominant ET process observed.

Section 4: WS_2 PL map region for PL scatter data shown in Figure 5.a

WS_2 PL scatter data presented in Figure 5.a were measured from the *64 µm x 48 µm* rectangular region (orange dashed lines) shown in the optical images of the monolayer below.

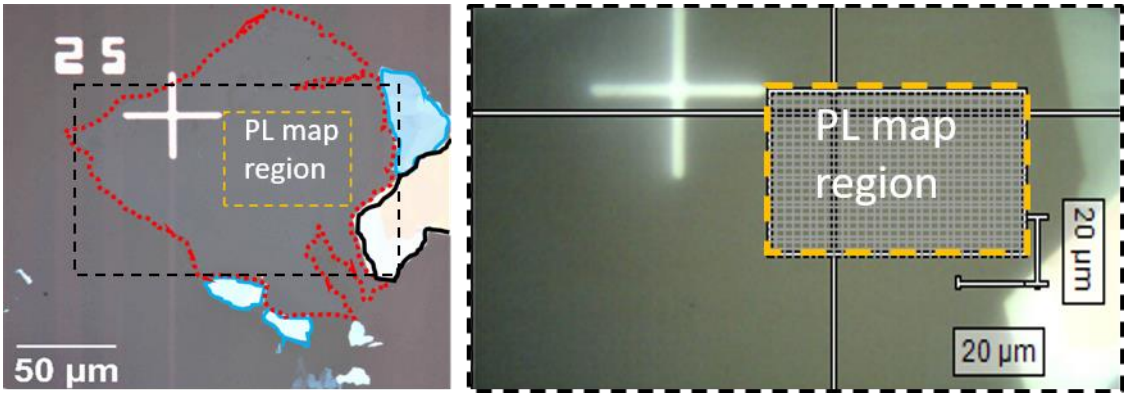

SI Fig 4:. LHS image shows monolayer region outlined in red dashed lines and estimated region of PL map is outlined in orange dashed lines. Black dashed region in LHS corresponds zoomed optical image on RHS taken with the Invia microscope described in the *experimental section* of the manuscript. Orange dashed lined in RHS represents actual 64 *µ*m × 48 *µ*m PL map region taken with invia microscope (see *experimental section)*. White mesh in RHS represents PL map resolution (2 *µm* × 2 *µm*) as described in *experimental section*.

Section 5: Energy Transfer efficiency derivation

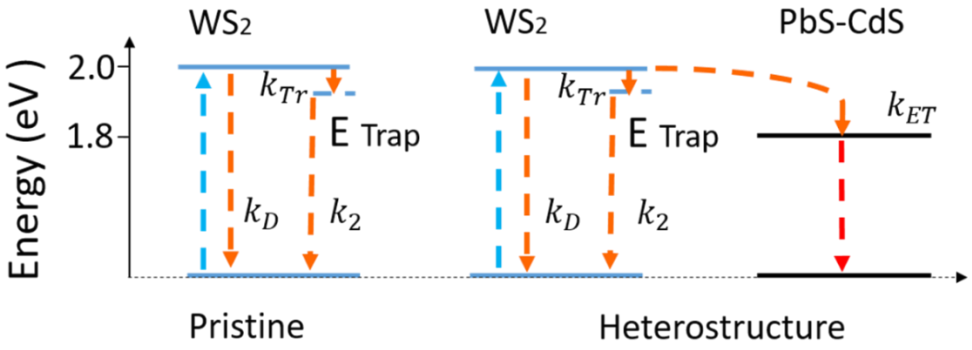

SI Fig 5: Energy level diagram illustrating radiative exciton pathways in pristine WS_2 (LHS) and in heterostructure. Blue arrows represent initial excitation, orange arrows represent WS_2 excitons and red arrows represent down-shifted excitons that recombine at lower energy in the PbS-CdS QD.

Table 2: Fitted PL lifetimes of pristine and heterostructure samples and resulting estimates for ET efficiencies. Fast components of WS_2 PL decay in heterostructure τ_1' and transfer efficiencies η_{ET} represent upper bound values due to limitations in instrument sensitivity.

Intensity	Pristine τ_1	Heterostructure τ_1'	Pristine τ_2	Heterostructure τ_2'
0.21 W cm^{-2}	0.456 ns	0.26 ns	3.63 ns	3.64 ns
63.4 W cm^{-2}	0.62 ns	0.26 ns	2.95 ns	2.9 ns

Following the RHS of SI Figure 5. WS_2 donor PL kinetics in the heterostructure can be described *via* the following set of related ordinary differential equations (ODEs):

$$\frac{dD^*}{dt} = -(k_D + k_{TR} + k_{ET})D^* \quad (12)$$

$$\frac{dTr}{dt} = k_{TR}D^* - k_2 Tr \quad (13)$$

Where D^* and Tr represent the WS_2 donor and trap state exciton populations respectively. The constants k_D, k_{TR}, k_{ET} and k_2 represent the donor's intrinsic recombination rate; intrinsic trapping rate; donor-acceptor energy transfer (ET) rate; and trap-ground state recombination rate respectively. By integration we arrive at the solutions to *equations 12* and *13*.

$$D^*(t) = D_0^* e^{-(k_D + k_{TR} + k_{ET})t} \quad (14)$$

$$Tr(t) = \frac{k_{TR}D_0^*}{[k_2 - (k_D + k_{TR} + k_{ET})]}\left(e^{-(k_D+k_{TR}+k_{ET})t} - e^{-k_2 t}\right) \quad (15)$$

Where D^*_0 represents the initial donor population. As such, the PL dynamics in the heterostructure can be defined as the sum of donor and trap population decay terms given by equations *14* and *15*:

$$PL(t) = D^*(t) + Tr(t) \quad (16)$$

i.e.

$$PL(t) = D_0^* e^{-(k_D+k_{TR}+k_{ET})t} + \left(\frac{k_{TR}D_0^*}{[k_2 - (k_D + k_{TR} + k_{ET})]}\left(e^{-(k_D+k_{TR}+k_{ET})t} - e^{-k_2 t}\right)\right) \quad (17)$$

In the absence of the QD acceptor the pristine WS_2 kinetics can be modelled by setting the transfer term $k_{ET} = 0$ so that:

$$PL(t) = D_0^* e^{-(k_D+k_{TR})t} + \left(\frac{k_{TR}D_0^*}{[k_2 - (k_D + k_{TR})]}\left(e^{-(k_D+k_{TR})t} - e^{-k_2 t}\right)\right) \quad (18)$$

The PL dynamics described by equations 17 and 18 consist of fast and slow decay components. In the pristine case (equation 18), at short time, *i.e.* t → 0, the fast decay time is given by:

$$\tau_1 \sim {}^{1}/_{(k_D + k_{TR})} \quad (19)$$

Similarly, in the heterostructure case (equation 17):

$$\tau_1' \sim {}^{1}/_{(k_D + k_{TR} + k_{ET})} \quad (20)$$

At long time *i.e.* t → ∞, given that the slow decay component (τ_2) remains unchanged for a given fluence (see Table 2), the slow decay time in both pristine and heterostructure cases is given as:

$$\tau_2 \sim \tau_2' \sim {}^{1}/_{(k_2)} \quad (21)$$

From equations 19 and 20, we can deduce the ET rate, k_{ET}, as:

$$k_{ET} = (k_D + k_{TR} + k_{ET}) - (k_D + k_{TR}) \quad (22)$$

The ET efficiency can then be determined in terms of rate constants. Using *equations 19, 20* and *22*, the ET can be simplified in terms of fast decay time constants as shown in *equation 2* of the main text:

$$\eta_{ET} = \frac{k_{ET}}{(k_D + k_{TR} + k_{ET})} = 1 - \frac{\tau_1'}{\tau_1} \quad (23)$$

Section 6: QD PL image on TMD monolayer

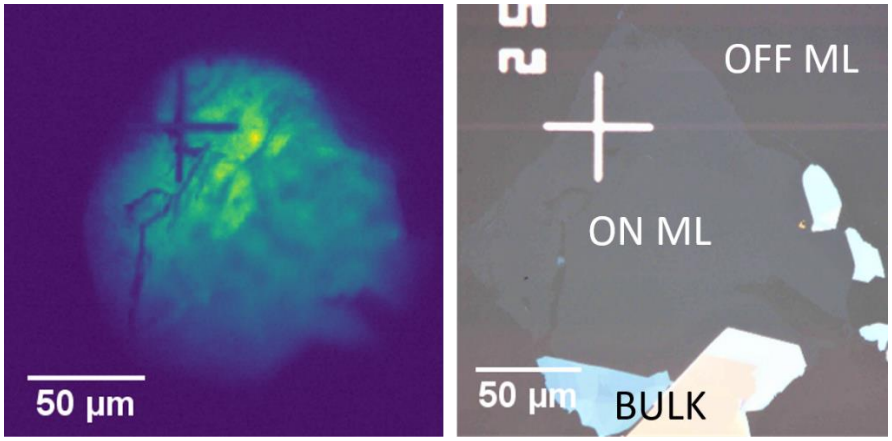

SI Fig 6: (LHS) Wide-field QD PL (900 nm) image of heterostructure at 620 nm excitation. (RHS) Optical image of monolayer used in heterostructure. QD PL clearly enhanced on TMD monolayer.

References

(1) Del Valle, J. C.; Catalán, J. Kasha's Rule: A Reappraisal. *Phys. Chem.* **2019**, *21*, 10061–10069. https://doi.org/10.1039/c9cp00739c.

(2) Mispelon, A.; Yan, J.; Milani, A. H.; Chen, M.; Wang, W.; O'Brien, P.; Saunders, B. R. Effects of Added Thiol Ligand Structure on Aggregation of Non-Aqueous ZnO Dispersions and Morphology of Spin-Coated Films. *RSC Adv.* **2015**, *5*, 18565–18577. https://doi.org/10.1039/c4ra15013a.

(3) Liu, Y.; Gibbs, M.; Puthussery, J.; Gaik, S.; Ihly, R.; Hillhouse, H. W.; Law, M. Dependence of Carrier Mobility on Nanocrystal Size and Ligand Length in PbSe Nanocrystal Solids. *Nano Lett.* **2010**, *10*, 1960–1969. https://doi.org/10.1021/nl101284k.

(4) Förster, T. Transfer Mechanisms of Electronic Excitation. *Discuss. Faraday Soc.* **1959**, *27*, 7–17.

(5) Guzelturk, B.; Demir, H. V. Near-Field Energy Transfer Using Nanoemitters For Optoelectronics. *Adv. Funct. Mater.* **2016**, *26*, 8158–8177. https://doi.org/10.1002/adfm.201603311.

(6) Hernández-Martínez, P. L.; Govorov, A. O.; Demir, H. V. Generalized Theory of Förster-Type Nonradiative Energy Transfer in Nanostructures with Mixed Dimensionality. *J. Phys. Chem. C* **2013**, *117*, 10203–10212. https://doi.org/10.1021/jp402242y.

(7) Melle, S.; Calderón, O. G.; Laurenti, M.; Mendez-Gonzalez, D.; Egatz-Gómez, A.; López-Cabarcos, E.; Cabrera-Granado, E.; Díaz, E.; Rubio-Retama, J. Förster Resonance Energy Transfer Distance Dependence from Upconverting Nanoparticles to Quantum Dots. *J. Phys.*

Chem. C **2018**, *122*, 18751–18758. https://doi.org/10.1021/acs.jpcc.8b04908.

(8) Moreels, I.; Lambert, K.; Smeets, D.; De Muynck, D.; Nollet, T.; Martins, J. C.; Vanhaecke, F.; Vantomme, A.; Delerue, C.; Allan, G.; Hens, Z. Size-Dependent Optical Properties of Colloidal PbS Quantum Dots. *ACS Nano* **2009**, *3*, 3023–3030. https://doi.org/10.1021/nn900863a.

(9) Neo, M. S.; Venkatram, N.; Li, G. S.; Chin, W. S.; Ji, W. Synthesis of PbS/CdS Core-Shell QDs and Their Nonlinear Optical Properties. *J. Phys. Chem. C* **2010**, *114*, 18037–18044. https://doi.org/10.1021/jp104311j.